



Article

Shear Bond Performance of UHPC-to-NC Interfaces with Varying Sizes: Experimental and Numerical Evaluations

Shaohua He ¹, Xu Huang ¹, Jiale Huang ¹, Youyou Zhang ^{2,*}, Zhiyong Wan ³ and Zhitao Yu ¹

¹ School of Civil and Transportation Engineering, Guangdong University of Technology, Guangzhou 510006, China; hesh@gdut.edu.cn (S.H.); gduthx@mail2.gdut.edu.cn (X.H.); 15875747201@163.com (J.H.); yuzt@gdut.edu.cn (Z.Y.)

² Department of Civil Engineering, School of Human Settlements and Civil Engineering, Xi'an Jiaotong University, Xi'an 710049, China

³ Guangdong Communication Planning & Design Institute Group Co., Ltd., Guangzhou 510507, China; wanzhiyong@ghdi.cn

* Correspondence: youyouzhang@xjtu.edu.cn

Abstract: This paper explores the effect of bonding size on the shear performance of ultra-high-performance concrete (UHPC) and normal concrete (NC). The study includes two sets of direct shear tests on a total of 16 Z-shaped UHPC-NC bonded specimens. The first set consists of eight direct shear tests on the chiseled UHPC-NC interface with an average roughness of 4 mm (referred to as series C), from the authors' previous study. The second set involves eight direct shear tests on the chiseled UHPC-NC interface with additional short shear steel rebars (referred to as series CS) that possess identical roughness to the first set of tests. The study discusses the failure modes, shear stress–slip behavior, and strain histories of the UHPC-NC interfaces with varying bonding sizes and shear mechanisms. A finite element model incorporating the cohesive zone model for the UHPC-NC interface was developed to gain insights into the shear bond evolutions. Our experimental results show that the two sets of direct shear specimens exhibit similar size effects in the shear stiffness, bonding strength, and interfacial slippage of the UHPC-NC interface. The use of shear steel rebars mitigated the impact of interfacial size on the bond shear behavior, thereby enhancing shear stiffness and reducing susceptibility to brittle damage. Numerical simulations indicate that the shear stress inhomogeneity coefficients for the CS specimens with bonding heights of 100 mm, 200 mm, 330 mm, and 440 mm were 1.2%, 1.8%, 11.9%, and 17.4%, respectively. The findings of this study provide valuable insights for optimizing UHPC applications in the repair and strengthening of concrete structures.

Keywords: UHPC-NC interface; size effect; shear strength; direct shear test; cohesive simulation



Citation: He, S.; Huang, X.; Huang, J.; Zhang, Y.; Wan, Z.; Yu, Z. Shear Bond Performance of UHPC-to-NC Interfaces with Varying Sizes: Experimental and Numerical Evaluations. *Buildings* **2024**, *14*, 3684. <https://doi.org/10.3390/buildings14113684>

Academic Editor: Vipul Patel

Received: 2 November 2024

Revised: 17 November 2024

Accepted: 18 November 2024

Published: 19 November 2024



Copyright: © 2024 by the authors. Licensee MDPI, Basel, Switzerland. This article is an open access article distributed under the terms and conditions of the Creative Commons Attribution (CC BY) license (<https://creativecommons.org/licenses/by/4.0/>).

1. Introduction

The deterioration of concrete bridges resulting from prolonged exposure to harsh environments and overloads has become a prevalent problem recently [1–3]. A statistical analysis of over two million concrete bridges worldwide indicates that over 34% are currently classified as structurally deficient [4]. In response to this challenge, engineers have sought to repair damaged and degraded concrete bridges by employing ultra-high-performance concrete (UHPC) repair technology, aiming for efficient and durable restoration. UHPC offers superior properties to normal concrete (NC), including ultra-high strength, toughness, and impermeability [5,6]. However, creating a reliable bond between UHPC and NC is a critical challenge in the repair process [7].

In engineering applications, two main interface treatments are used for the UHPC-NC bond. The first treatment includes roughening the NC substrate surface with an average depth of 2 to 4 mm, which has been employed in projects such as the Mud Creek Bridge Deck Rehabilitation Project in the United States, where it has been effective in restoring

functionality [8]. The second treatment involves implanting short steel rebars into the roughened NC substrates to enhance bonding properties. This approach has been observed in projects like Canada's Mission Bridge Abutment Performance Improvement Project [9]. Both treatments have demonstrated favorable bonding properties with UHPC under shear-dominated complex stress states [8,9]. However, in actual bridge rehabilitation projects, diverse repair requirements and dimensions are often encountered. As the bond interface size increases, assessing UHPC-NC bond performance becomes more complex due to various uncertainties such as concrete surface defects (e.g., laitance, microcracks, and unevenness), interfacial shrinkage stresses, and the influence of external load transfer at the interface, particularly in large-scale repair projects [10,11].

The current research on the UHPC-NC bond mainly focuses on the bonding strength of the two types of concrete. Muñoz et al. [12] conducted shear and tensile tests to examine the interfacial bonding properties of UHPC and NC. The results showed that the UHPC-NC bonding mechanical properties significantly exceed the recommended bearing capacity of repair materials according to ACI 546-06 [13]. Yu et al. [14] and Apostolinas et al. [15] utilized bi-surface shear tests with interfacial roughness as a testing parameter. Their findings revealed that interface roughness significantly influences the bond strength of UHPC-NC, indicating a positive correlation between surface roughness and external load. Zhang et al. [16] studied UHPC-NC bond interface properties under different conditions. They found that the interfacial bond strength peaked at a 28-day curing age for UHPC. Proper wetting of the substrate interface increased the slant shear strength and split tensile strength of the UHPC-NC bond interface by 44.6% and 24.5%, respectively, compared to dry interfaces. Farzad et al. [17] evaluated the UHPC-NC bond interface, employing both experimental and numerical methods to determine the critical parameters for the interfaces. Their analysis yielded a maximum error of 18%, significantly lower than the 150% maximum error associated with the "Tie" model. In general, the existing research has predominantly focused on examining factors related to consistent interface dimensions, with minimal attention given to the impact of interface sizes. The influence of interface sizes on the shear bond performance of UHPC-NC interfaces has yet to be addressed.

Currently, studies on the size effects of concrete have predominantly concentrated on the material and structural levels. At the material level, the size effect of concrete is influenced by factors such as aggregate particle size and the random distribution of initial defects. This has been investigated through experiments and mesoscale simulations, leading to the development of representative size effect theories, including Weibull's statistical theory, Bazant's energy release criterion, and Carpinteri's fractal characteristics of cracks [18,19]. On the structural level, previous studies on the mechanical properties of concrete members, such as beams and columns, have shown a significant size effect on their mechanical properties [20–22]. Regarding the influence of geometric size on the bond strength between concrete members, Fang et al. [23] utilized a direct shear test to evaluate the shear bond at the interface between new and old NC slabs while varying bonding heights. The results indicate that the interfacial bond between the NC became more stable with increased bonding heights. Additionally, He et al. [24] investigated the influence of bonding heights on the tensile and shear strength at the chiseled interface between UHPC and NC. Their research reported that the interfacial bond between the UHPC and NC members changed with variations in interface size under shear and tensile conditions.

In order to examine the size effect the bond shear of UHPC-NC interfaces, this paper expands on a previous investigation [24] by performing direct shear tests with extra steel rebar implantation on the chiseled NC substrate surfaces. The study involved analyzing the results obtained from sixteen UHPC-NC bond tests, which included eight tests on the chiseled UHPC-NC interface conducted previously [24] and eight newly conducted direct shear tests on the chiseled UHPC-NC interface with short shear steel rebars. The main focus was to analyze the failure mode, stress–slip relationship, and strain history under shear loads. The size effects of the interfaces' shear stiffness, bonding strength, and relative slip are determined based on the experimental observations. Additionally, finite element

(FE) models were established for calibration, and the relationship between bond size and stress field distribution was determined, providing valuable insights for evaluating the performance of UHPC-NC bond interfaces.

2. Experimental Works

2.1. Test Specimens

Figure 1 illustrates the setup of the Z-shaped direct shear specimens, which are commonly used to evaluate the shear strength at the concrete bonded surfaces [23,24]. The setup involves an inverted pair of L-shaped concrete blocks, with the combined area of UHPC and NC positioned at the center of the specimen. The UHPC-NC bond interfaces were prepared in two ways: (a) Chiseling (C): This involved a roughing process using a pneumatic tool to an average depth of 4 mm and (b) Chiseling and steel rebar dowels (CS): Holes were drilled into the chiseled interface (with identical roughness to C), and shear steel rebars were inserted into the holes and anchored using epoxy adhesive.

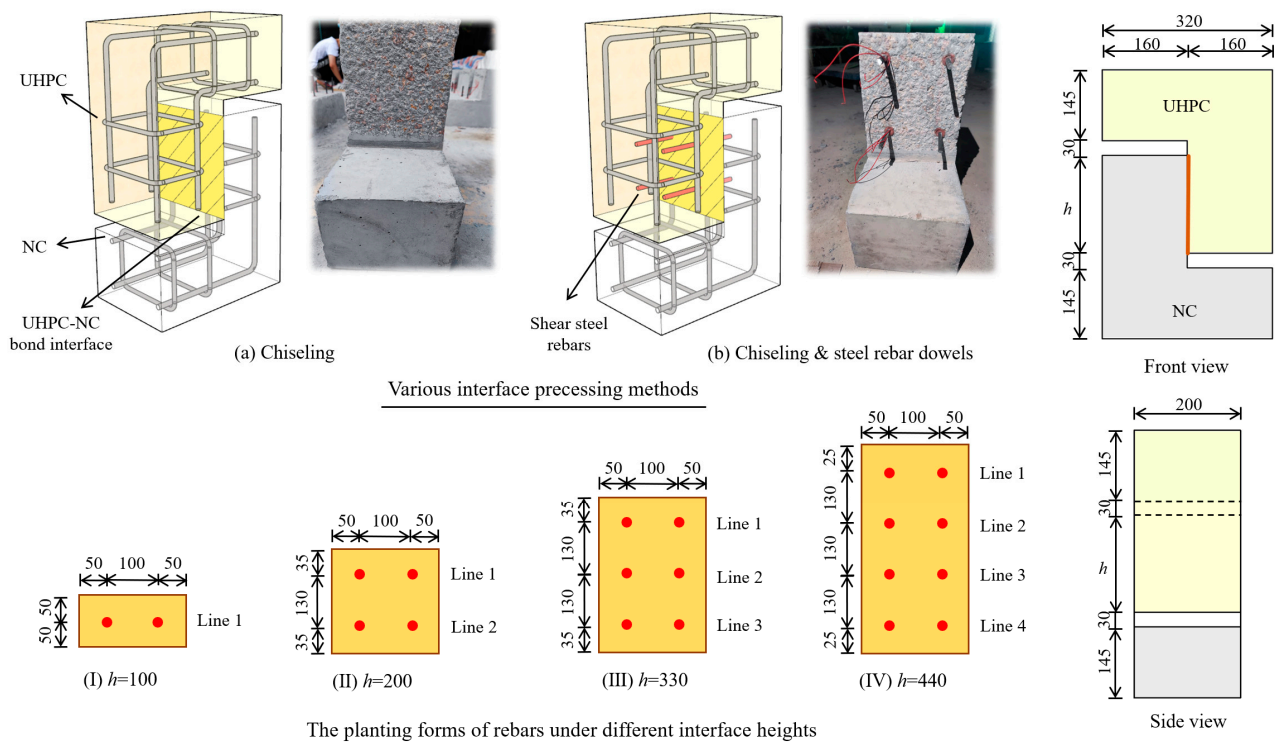


Figure 1. Main configuration of direct shear specimens (unit: mm).

Table 1 provides an overview of the key parameters for the direct shear test specimens. Two series of direct shear tests were conducted, each consisting of four different bonding heights with two identical samples per height, resulting in a total of 16 UHPC-NC specimens. The test series is categorized as C (previously conducted) and CS (newly conducted), denoting the UHPC-NC bond interfaces treated with chiseling and chiseling and implanted rebars, respectively. In the specimen codes, “UN” represents a combination of UHPC and NC, and “H” represents the bond interface height, with the following digit donating the height value. For example, the code “UN-C-H100” refers to a direct shear specimen with an interface height of 100 mm, where the UHPC-NC bond interface has been treated with chiseling.

The preparation of the UHPC-NC bond specimens involves five steps, as illustrated in Figure 2: (a) prepare the formwork and steel rebars; (b) cast and cure the NC substrate for 28 days; (c) roughen the NC substrates with an average depth of 4 mm using pneumatic tools; (d) for the CS series, drill holes in the roughened surface and implant steel rebars; (e) and wet the treated surface, cast the UHPC, and cure for 28 days.

Table 1. Basic parameters of direct shear tests.

Series	Specimen Code	Number	Interface Treatment	Interface Size (mm)		Average Roughness (mm)	Implanted Shear Rebar Ratio
				h	w		
Previous test: C [24]	UN-C-H100	2	Chiseling	100	200	4	0
	UN-C-H200	2		200			
	UN-C-H330	2		330			
	UN-C-H440	2		440			
Current test: CS	UN-CS-H100	2	Chiseling and implanted steel rebars	100	200	4	0.5%
	UN-CS-H200	2		200			
	UN-CS-H330	2		330			
	UN-CS-H440	2		440			

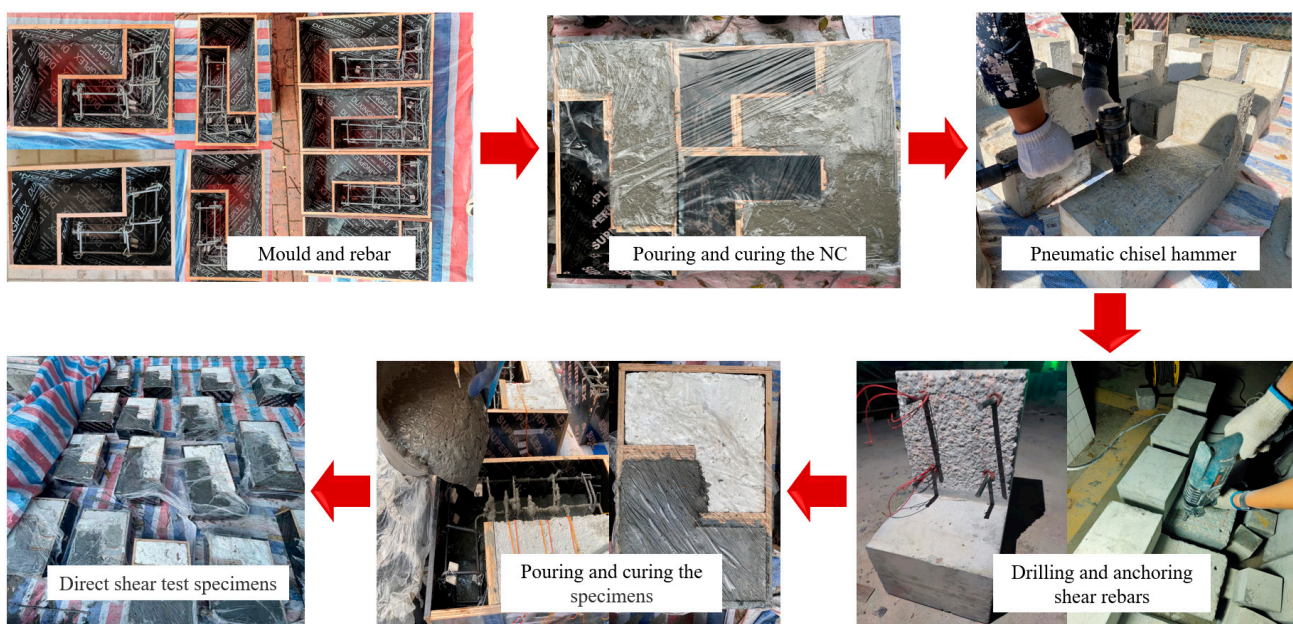


Figure 2. Fabrication process of direct shear specimens.

2.2. Material Properties

The NC blocks were made with C50 grade concrete (target cubic compressive strength of 50 MPa), while the UHPC used a commercial premix of grade RPC120 (target cubic compressive strength of 120 MPa), as detailed in Table 2. The concrete's material properties were determined according to Chinese codes [25–27]. Specifically, the cubic compressive strength of the NC and UHPC were determined by testing six cubes with a length of 150 mm and 100 mm, respectively. The prismatic compressive strength and elastic modulus were tested using twelve prism samples, with a size of 150.0 mm × 150.0 mm × 300.0 mm for NC and 100.0 mm × 100.0 mm × 300.0 mm for UHPC. All cubes and prisms were maintained for 28 days, along with the direct shear specimens. The steel stirrups and shear steel rebars were made of grade HRB400 rebars, which were tested according to GB/T 228.1-2010 [28]. The mechanical properties of the NC, UHPC, and rebars are shown in Table 3.

Table 2. Mix proportions of NC and UHPC (kg/m³).

Material	Cement	Coarse Aggregate	Sand	Superplasticizer	Water	Silica Fume	Quartz Powder	Quartz Sand	Steel Fiber
NC	470	1060	710	1.8	155	-	-	-	-
UHPC	771.2	-	-	20.1	180.5	154.2	154.2	848.4	235.5

Table 3. Summary of material properties (MPa).

Material	Cubic Compressive Strength	Prismatic Compressive Strength	Yield Strength	Ultimate Strength	Elastic Modulus ($\times 10^3$)
NC	62.0	52.3	-	-	38.3
UHPC	127	106	-	-	44.2
HRB 400	-	-	483	594	200

2.3. Test Setup and Instrumentation

Figure 3 shows the loading equipment and test arrangements. The specimens underwent testing using a servo-hydraulic press, with displacement loading applied at a rate of 0.1 mm/min to accurately capture the interface mechanical response. A steel plate was carefully placed on top of the specimen, and any gaps were filled with gypsum to ensure that the stress from the testing machine was uniformly distributed to the specimen. The bond interface of the specimens was aligned with the loading center. Two linear variable differential transformers (LVDTs) were used to monitor the displacements at the interface, positioned vertically near the gaps between the concrete blocks to record vertical slip at the interface. In addition, two strain gauges were placed near the interface to capture strain development closely. Strain gauges were also attached along both sides near the interface to monitor the mechanical response of the shear rebars.

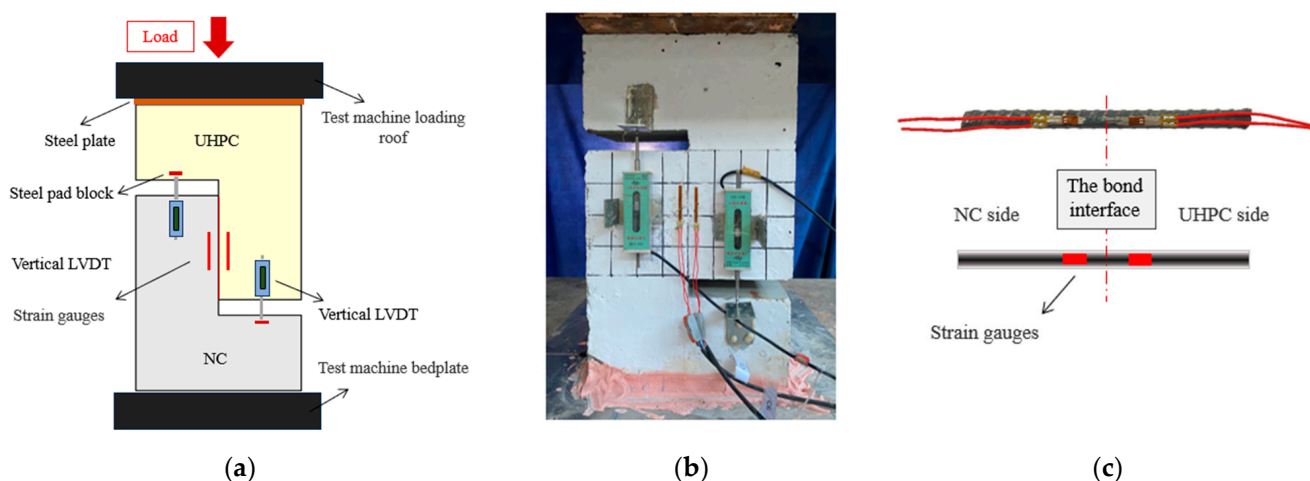


Figure 3. Test device and instrumentation arrangement: (a) test device and specimen arrangement; (b) the specimen layout; (c) strain detection of shear steel rebars.

3. Experimental Results and Discussion

3.1. General Results

The results of the direct shear specimens are summarized in Table 4. The average shear stress at the UHPC-NC bond interface under direct shear loading was calculated by dividing the applied load by the bonded area. In this table, the shear stress and slip corresponding to the cracking load F_c are defined as the cracking shear strength τ_c and cracking shear slip $S_{c,r}$, respectively. Similarly, the shear stress and slip corresponding to the ultimate load F_u are defined as the ultimate shear strength τ_u and ultimate shear slip $S_{u,r}$, respectively. The shear stress and slip corresponding to the residual load F_r are defined as the residual shear strength τ_r and residual shear slip $S_{r,r}$. It is worth noting that because the C specimens failed in a brittle manner, the cracking load is considered to be the ultimate load.

The failure modes of the UHPC-NC bond specimens are depicted in Figure 4. In Figure 4a, two typical failure modes of the series C specimens are observed: (i) partial interface failure (P), where fracture occurs in the UHPC-NC transition zone with part of the NC adhering to damaged surfaces, and (ii) complete NC failure (F), where crushing

or fracture occurs at the NC side and the interface remains intact. Mode P occurred in UHPC-NC interfaces with large bonding heights ($H = 330$ mm and 440 mm), while Mode F dominated in smaller ones ($H = 100$ mm and 200 mm). In larger specimens, interfacial shear is often accompanied by a non-uniform distribution of normal stresses, with longer fracture regions amplifying stress heterogeneity [23]. This uneven stress distribution can create localized regions prone to damage under positive normal stresses, potentially leading to normal separation at the interface [29–31]. Moreover, the mechanical interlocking of the interface may be underutilized, resulting in a mixed mode of interfacial damage.

Table 4. Summary of direct shear test results.

Label	Specimen Number	F_c (kN)	τ_c (MPa)	S_c (mm)	F_u (kN)	τ_u (MPa)	S_u (mm)	F_r (kN)	τ_r (MPa)	S_r (mm)
UN-C-H100	Spec. 1	54.30	2.72	0.236						
	Spec. 2	59.40	2.97	0.267						
UN-C-H200	Spec. 1	120.53	3.01	0.287						
	Spec. 2	125.20	3.13	0.299						
UN-C-H330	Spec. 1	246.94	3.74	0.485						
	Spec. 2	258.60	3.92	0.510						
UN-C-H440	Spec. 1	278.00	3.16	0.543						
	Spec. 2	294.20	3.34	0.630						
UN-CS-H100	Spec. 1	43.20	2.16	0.174	75.61	3.78	0.408	55.09	2.74	0.638
	Spec. 2	48.40	2.42	0.194	73.20	3.66	0.399	53.49	2.72	0.693
UN-CS-H200	Spec. 1	105.22	2.63	0.238	155.87	3.90	0.548	117.01	2.93	0.891
	Spec. 2	107.10	2.68	0.235	162.00	4.05	0.566	114.50	2.86	0.993
UN-CS-H330	Spec. 1	186.90	2.83	0.341	274.55	4.16	0.730	197.83	3.00	1.224
	Spec. 2	183.73	2.79	0.347	258.19	3.91	0.693	179.61	2.72	1.197
UN-CS-H440	Spec. 1	297.00	3.38	0.500	394.30	4.48	0.885	277.40	3.15	1.587
	Spec. 2	301.70	3.43	0.591	383.90	4.36	0.902	268.30	3.05	1.578



(a)



(b)

Figure 4. Typical failure modes of the direct shear specimens: (a) C specimens and (b) CS specimens.

Concerning the failure of series CS specimens, Figure 4b illustrates that all specimens displayed partial interfacial failure (P). Except for UN-CS-H100, which has a 100 mm interface height and experienced shearing of interfacial rebars during loading, the other specimens did not exhibit complete fracture of the rebars. During the loading process, a crack first appeared at both ends of the interface, and it slowly spread from the ends toward the middle as slippage intensified, ultimately fully penetrating the interface. This demonstrates the significant role of shear rebars in improving stress transfer and distribution in the bond area, especially for smaller interface sizes, and in facilitating the transfer of shear stresses to the UHPC. Furthermore, interfacial rebars in the transition zone between the UHPC and NC can mitigate the effects of shear stresses on the NC side, which potentially reduces the influence of the interfacial size.

3.2. Shear Stress vs. Interfacial Slippage Relationship

Figure 5 shows the shear stress–interfacial slip curves for the UHPC-NC specimens. The experimental curves from previously tested chiseled interfaces are also included for analysis. It should be noted that shear stress is the average stress at the interface, calculated by dividing the applied load by the bonding area. The slippage corresponds to the vertical displacement recorded by the LVDTs (see Figure 3b). The direct shear specimens show minimal variation in the shear stress–slip relationship across the same test series, despite differences in bonding heights. The C-series demonstrates a nearly linear shear stress–slip relationship because it features a chiseled interface, which results in brittle failure characteristics. In contrast, the CS-series exhibits nonlinear relationships, with all specimens displaying a more ductile failure mode due to the implanted rebars. Figure 5a shows that the chiseled specimens in series C display a linear relationship between shear stress and slippage during loading, with a sudden drop in shear stress upon reaching peak load due to detachment. This phenomenon can be attributed to the brittle failure occurring at the chiseling interface, which leads to rapid cracking and failure within moments. In comparison, Figure 5b shows that adding steel rebars to the chiseled interface significantly changes the slipping behavior. The main features in the stress–slippage curves for the CS specimens are similar regardless of the varied bonding heights. Accordingly, a shear bond-slip model is derived and consists of four phases, as displayed in Figure 5a: (i) the initial elastic increasing phase, where relative slip linearly develops with shear stress due to the shear deformation of the concrete at the transition zone; (ii) the elastic–plastic phase, where relative slip accelerates with shear stress due to cracking at the interface; (iii) the post-failure degradation phase, where shear stress drops while slip sharply increases due to plastic deformation of the interfacial rebars; and (iv) the failure residual phase, where nearly constant residual stress was maintained with increasing relative slip. In general, the mechanical behavior of the bond interface undergoes significant changes after adding steel rebars to the interface, particularly in the initial elastic phase.

3.3. Shear Stress vs. Interfacial Strain Relationship

Figure 6 shows the shear stress–strain curves for the concrete at the transition zone of the interface. The shear stress is calculated by dividing the applied load by the bonding area. The strain is measured using gauges attached near the UHPC-NC interface (refer to Figure 3a). As shown in Figure 6a, similar to the slipping curves, series C specimens with a chiseled interface exhibit a linear strain development with the shear stress, which aligns well with the brittle failure feature of the specimens. It is worth noting that the interfacial strain in specimens UN-C-100 and UN-C-200 increases much faster than in specimens UN-C-330 and UN-C-440. This is understandable as specimens UN-C-330 and UN-C-440 have longer load-transferring paths between the UHPC and NC blocks compared to the former specimens, leading to slower strain development at the middle point of the bonding height, which is where the strain gauges are positioned.

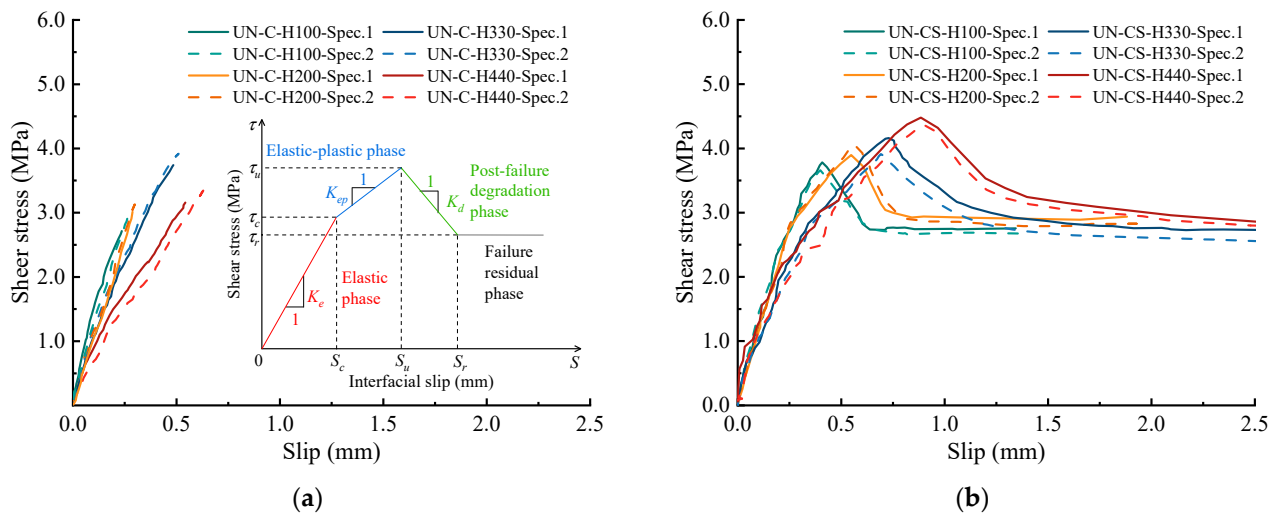


Figure 5. Shear stress vs. slip relationship: (a) Series C with the chiseled interface [24]; (b) Series CS with implanted rebar in the chiseled interface.

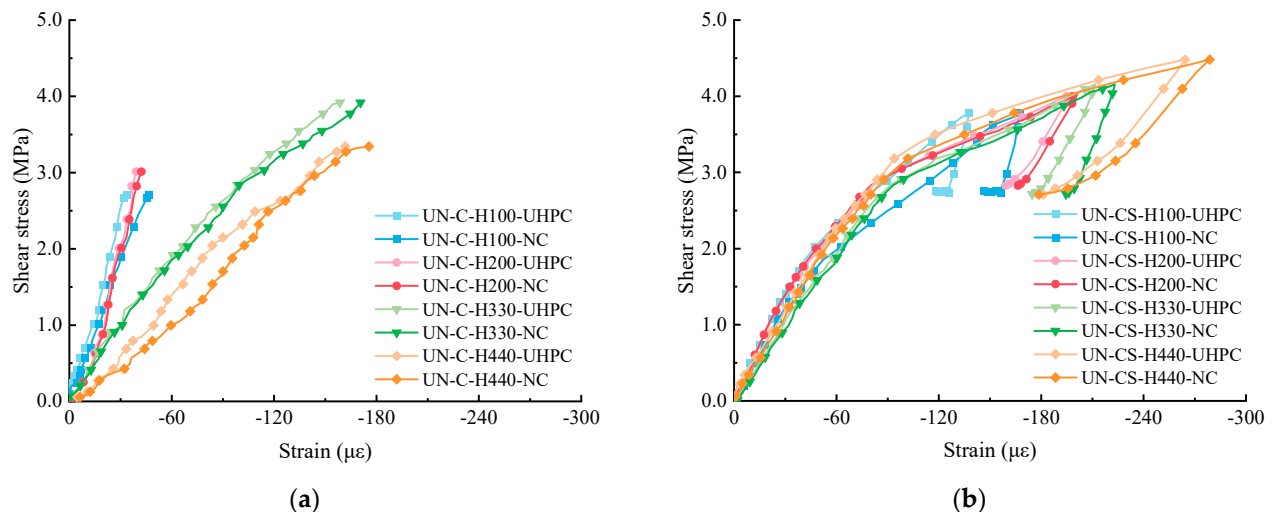


Figure 6. Interfacial shear stress vs. strain curves: (a) Series C with the chiseled interface [24]; (b) Series CS with implanted rebar in the chiseled interface.

Figure 6b shows the shear stress–strain curves from the CS specimens. It is evident that the stress–strain curves of the CS specimens with interfacial steel rebars almost overlap, despite variations in bonding height. An obvious knee point is identified at a stress level of approximately 3.0 MPa, indicating that the UHPC-NC interfaces entered their elastic–plastic phase under shear stress. This is consistent with the shear stress–interfacial slip curves shown in Figure 5b. Beyond this knee point, the chemical adhesion at the interface gradually diminishes due to cracking on the contacting surfaces. The shear loads are supported by mechanical interlocking, friction, and rebar dowels. The rapid increase in strains during the elastic–plastic phase is attributed to the concentrated loads from the implanted steel rebars, causing an increase in concrete strains at the transition zone. Rebar implantation resulted in a more uniform strain distribution across different bonding heights and reduced the size influence, especially in UN-C-100 and UN-C-200. The maximum interfacial strain exceeded $180 \mu\epsilon$, demonstrating improved bond shear performance.

3.4. Strains in the Interfacial Shear Rebars

Figure 7 illustrates the shear stress–strain curves of the steel rebars embedded at the interface of UHPC-NC in CS specimens. The strain in the shear rebars demonstrates a con-

sistent increasing trend across all specimens. Initially, the rebar strains increase linearly with the applied shear stress before concrete cracking, indicating the simultaneous activation of the chemical bond and implanted steel rebars under shear loads. Subsequently, a sudden increase in rebar strain is observed in the shear stress–strain curves for all specimens upon reaching the cracking load, suggesting the predominant role of the steel rebars in resisting shear loads. It is worth noting that strains in the rebar on the NC side increase faster than on the UHPC side, irrespective of interface size. This is attributed to stress redistribution on the NC side after concrete cracking, allowing more shear stress to be dispersed by the interfacial steel rebars and delaying the cracking process. Furthermore, the cracking process resulted in the weakening of the separation effect of the concrete blocks, which was caused by the anchoring of the rebars. This maintained a continuous growth of slip, effectively absorbing the shear stresses and providing a sustainable strain accumulation.

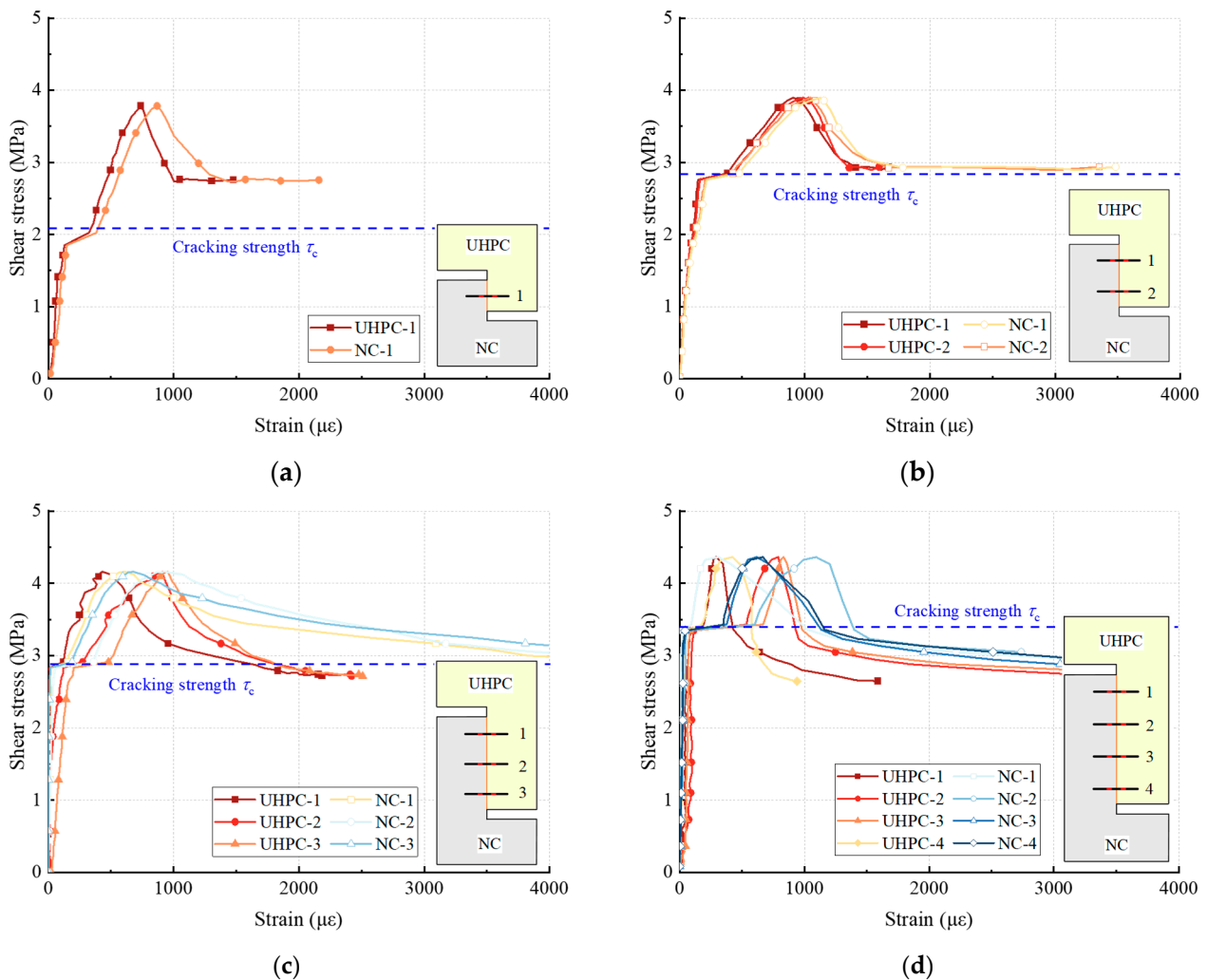


Figure 7. Shear stress–strain curves for interfacial steel rebars: (a) UN-CS-H100; (b) UN-CS-H200; (c) UN-CS-H330; (d) UN-CS-H440.

4. Influence of Bonding Size on UHPC-NC Shear Properties

4.1. The Size Effect in Interfacial Bonding Strength

Figure 8 illustrates the average bonding strength of the UHPC-NC interfaces at different shear-behaving stages. In series C, the ultimate bonding strength of the chiseled specimens corresponds to the cracking strength, as the interfaces' brittle cracking governs the specimen's ultimate failures. As shown in Figure 8, it is evident that with an increase in interface height from 100 mm to 440 mm, the cracking shear strength (τ_c) of the CS speci-

mens with the same interface height is 19.5%, 13.5%, 26.6%, and -4.8% lower compared to that of the C specimens. This difference may be attributed to stress concentration near the steel rebars at the interface, leading to earlier crack initiation in the concrete. Despite the differences in interface shear keys, there is a consistent increase in bond shear strength between UHPC and NC with higher bonding heights at the interface. Specifically, the average ultimate shear strength (τ_u) of UN-C-H200, UN-C-H330, and UN-C-H440 is 7.9%, 34.6%, and 14.2% higher than that of UN-C-H100. Similarly, the τ_u of UN-CS-H200, UN-CS-H330, and UN-CS-H440 shows improvements of 6.9%, 8.5%, and 18.8% compared to the baseline UN-CS-H100, and the corresponding improvements of residual shear strength (τ_r) also reach 6.0%, 4.8%, and 13.6%, respectively.

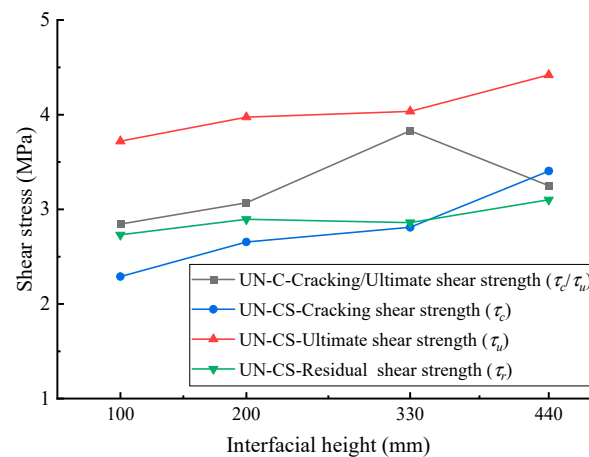


Figure 8. Influence of bonding height on interfacial shear stress.

The chiseled interfaces in series C showed more significant variations in strength than the series CS specimens. This is because the roughened interface in C specimens fails immediately upon cracking, leading to less uniform stress distribution and making the interface more sensitive to initial defects such as uneven roughness and micro-cracks. On the other hand, the chiseled interfaces with additional shear rebars in series CS exhibited ductile failure, allowing for more uniform cracking and enhancing mechanical interlock and frictional resistance across the interface. This reduces the impact of inherent defects at the interface. After cracking, the bond interface in CS specimens is mainly governed by stable frictional forces, which leads to a less significant size effect on residual strength. This indicates that implanting steel rebars at the interface can help reduce the adverse effects of interfacial defects.

4.2. The Size Effect in Interfacial Slippage

Figure 9 illustrates the interfacial slip of the UHPC-NC interfaces at different stages of shear behavior. An increase in interfacial slip is observed at the initial cracking load (S_c), ultimate load (S_u), and residual load (S_r) as the interface size increases. For instance, the ultimate slip (S_u) of UN-C-H200, UN-C-H330, and UN-C-H440 is 16.5%, 97.8%, and 133.2% higher than that of UN-C-H100. Similarly, the S_u of UN-CS-H200, UN-CS-H330, and UN-CS-H440 shows improvements of 38.2%, 76.6%, and 121.7% compared to UN-CS-H100, and the corresponding improvements of cracking slip (S_c) also reach 28.6%, 87.0%, and 196.6%, respectively. Additionally, for the interface with bonding heights of 100 mm, 200 mm, 330 mm, and 440 mm, the S_u of the CS specimens is 60.4%, 90.1%, 43.0%, and 52.3% larger than that of the C specimens. The significant increase in ductile damage with slip observed in CS specimens has also been reported in previous studies [32–34]. This behavior is attributed to the presence of steel rebars traversing the interface, which effectively facilitate load transfer during interfacial slip [35]. Consequently, this promotes a smoother distribution of shear stresses between the UHPC and NC blocks, resulting in a more ductile damage pattern and an extended interfacial fracture process.

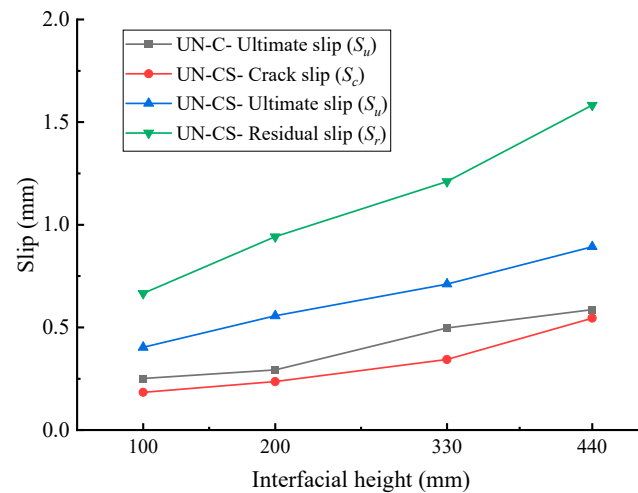


Figure 9. Influence of bonding height on interface slip.

4.3. The Size Effect in Interfacial Bond Shear Stiffness

Based on the simplified shear stress-interfacial slippage model described in Figure 5b, the bond shear stiffness at the UHPC-NC interface is established. This stiffness represents the shear modulus obtained from slip curves during different phases. The elastic shear stiffness (K_e) is the ratio of elastic stress to its corresponding strain, while the elastic–plastic shear stiffness (K_{ep}) is associated with the slope at the elastic–plastic phase of the slip curve. Figure 10 shows the influence of bonding height on the interfacial shear stiffness. When the bonding height of UN-C-H100 was increased from 100 mm to 200 mm, 330 mm, and 440 mm, the elastic stiffness (K_e) decreased by 7.4%, 31.9%, and 51.0%, respectively. Similarly, for UN-CS-H100, increasing the bonding height from 100 mm to 200 mm, 330 mm, and 440 mm decreased elastic stiffness (K_e) by 9.8%, 34.4%, and 49.9%, respectively. Moreover, the elastic–plastic shear stiffness (K_{ep}) decreased by 36.7%, 48.8%, and 55.2%, and the residual shear stiffness of the interface (K_d) also decreased by 25.7%, 37.6%, and 49.2%, respectively. This suggests that enlargement in the interface size led to corresponding decreases in shear stiffness. Although the initial load-carrying capacity increases, the larger interface results in greater slip accumulation, ultimately leading to a net decrease in shear stiffness. Additionally, the reduction in K_e was greater than in K_{ep} and K_d , indicating that the implanted rebars helped reduce the negative effects of increased bonding size.

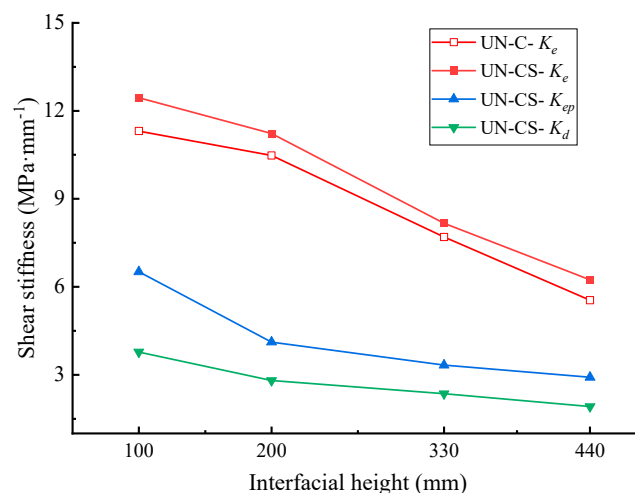


Figure 10. Effect of interface height on shear stiffness.

5. Numerical Works

5.1. Numerical Simulation of UHPC-NC Tests

5.1.1. Establishment of the FE Model

In order to assess the shear bond evolution at the UHPC-NC interface with different bonding sizes, a solid nonlinear finite element (FE) model of the direct shear specimens was created using ABAQUS (2021 version) software. The FE model is illustrated in Figure 11, using a specimen with an interface height of 200 mm as an example. The FE model comprises a UHPC block, an NC block, steel rebars, and a cohesive layer. The concrete blocks are simulated using the reduced-integration 8-node solid element (C3D8R), while the steel rebars are modeled using the truss element (T3D2). The UHPC-NC interface is represented by a 0-thickness three-dimensional cohesive element (COH3D8) that accommodates various traction-separation law curves. This cohesive zone model (CZM) is currently recognized as the most effective way to simulate bond damage processes [36–38]. A displacement-controlled loading method is used, where displacement is applied by coupling a virtual reference point to the specimen's top surface to prevent stress concentration. The mesh convergence study results led to a mesh size of 10 mm.

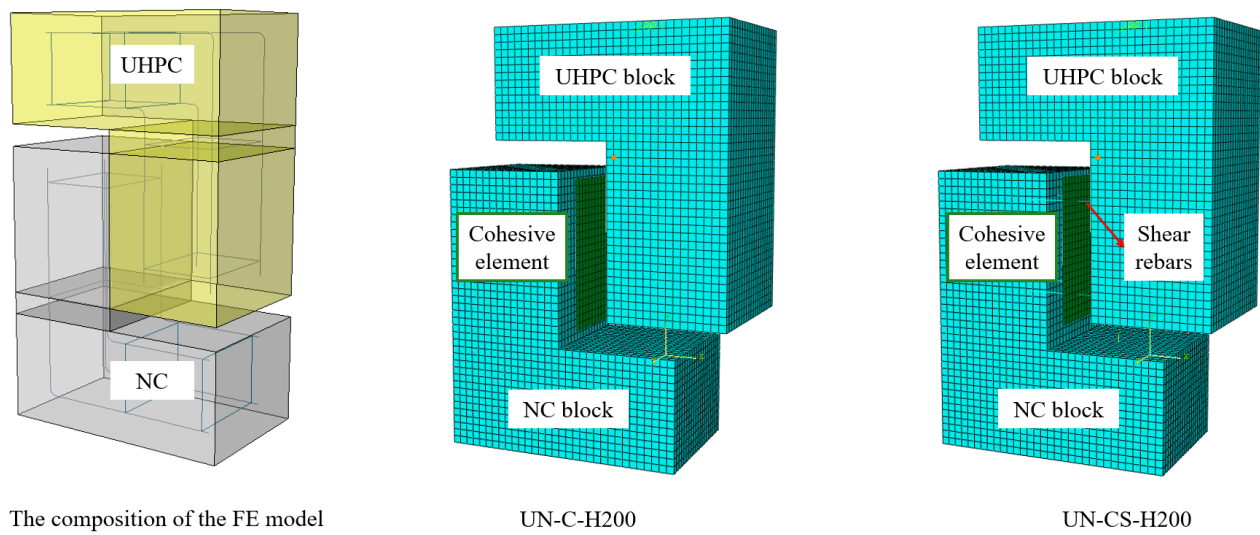


Figure 11. Composition and meshing of the FE model.

Figure 12 presents a summary of the constitutive models of the materials. The tensile and compressive models for UHPC are from Zhang et al. [39] and the French code [40]. The constitutive model for NC is recommended by Ding and Yu et al. [41,42]. Steel reinforcements use the bilinear kinematic hardening plasticity intrinsic model and the Von Mises yield criterion [43]. The CZM includes initial elasticity (part OA) and damage evolution (part AB) derived from a bilinear constitutive model [44], as shown in Figure 12d. The constitutive relationship in the elastic stage of the CZM can be expressed as follows [45]:

$$\begin{Bmatrix} \sigma_n \\ \sigma_s \\ \sigma_t \end{Bmatrix} = \begin{bmatrix} K_{nn} & K_{ns} & K_{nt} \\ K_{ns} & K_{ss} & K_{st} \\ K_{nt} & K_{st} & K_{tt} \end{bmatrix} \begin{Bmatrix} \delta_n \\ \delta_s \\ \delta_t \end{Bmatrix} \quad (1)$$

where σ_n , σ_s , and σ_t represent tensile, shear, and tear stresses, respectively, while δ_n , δ_s , and δ_t correspond to tensile, shear, and tear strains. Similarly, K_{nn} , K_{ss} , and K_{tt} denote tensile stiffness, shear stiffness, and tear stiffness, respectively. Notably, K_{ns} , K_{nt} , and K_{st} are set to zero. This is because the thickness of the cohesive unit is minimal, and normal deformations are disregarded [46].

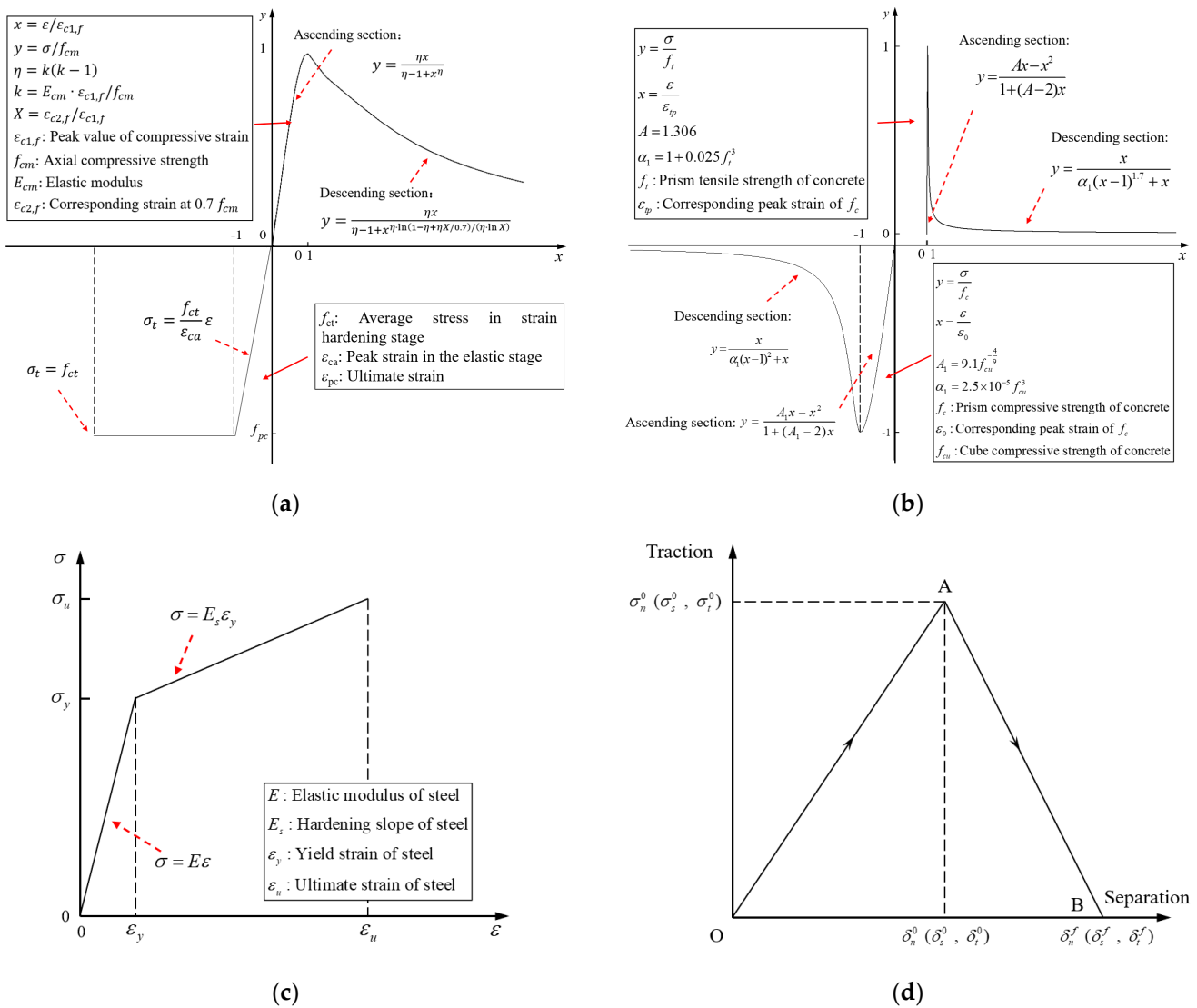


Figure 12. The constitutive model of the materials and the bond interface: (a) UHPC; (b) NC; (c) Steel; (d) CZM.

The damage onset criterion of the CZM is the quadratic nominal stress criterion, as expressed in Equation (2). In this context, σ_n^0 , σ_s^0 , and σ_t^0 denote the damage initiation stresses in the three directions of the cohesive element, respectively, and the meanings of $\langle \sigma_n \rangle$ are shown in Equation (3).

$$\left\{ \frac{\langle \sigma_n \rangle}{\sigma_n^0} \right\}^2 + \left\{ \frac{\sigma_s}{\sigma_s^0} \right\}^2 + \left\{ \frac{\sigma_t}{\sigma_t^0} \right\}^2 = 1 \tag{2}$$

$$\langle \sigma_n \rangle = \begin{cases} \sigma_n, & \sigma_n > 0 \\ 0, & \sigma_n \leq 0 \end{cases} \tag{3}$$

When the quadratic nominal stress criterion is in effect, the cohesive element begins to experience damage and stiffness degradation. At this point, the constitutive relationship for the damage evolution stage can be described as follows:

$$\begin{Bmatrix} \sigma_n \\ \sigma_s \\ \sigma_t \end{Bmatrix} = \begin{bmatrix} (1 - D)K_{nn} & 0 & 0 \\ 0 & (1 - D)K_{ss} & 0 \\ 0 & 0 & (1 - D)K_{tt} \end{bmatrix} \begin{Bmatrix} \delta_n \\ \delta_s \\ \delta_t \end{Bmatrix} \tag{4}$$

$$D = \frac{\delta_m^f (\delta_m^{\max} - \delta_m^0)}{\delta_m^{\max} (\delta_m^f - \delta_m^0)} \quad (5)$$

where D represents a value within the range of $[0, 1]$, with 0 indicating no damage to the material and 1 indicating complete failure of the material. The effective displacements at the onset of damage, the effective displacements at the eventual occurrence of damage, and the maximum effective displacements obtained during the loading process are represented by δ_m^0 , δ_m^f , and δ_m^{\max} , respectively. These values are obtained from the experimental loading history.

5.1.2. Feasibility Assessment

A comparison of the experimentally obtained shear stress–slippage curve with those produced by the FE models is presented in Figure 13a. For the C specimens, there is a strong correlation between the potential linear relationship and the FE calibration, and the shear stress distribution aligns well with the observed experimental phenomena. Similarly, the CS specimens also show a strong correlation in the load–displacement relationship, and the degradation of interface stiffness in the FE model during the elastic–plastic stage corresponds closely with the experimental outcomes. Additionally, to further verify the feasibility of using FE modeling technology, the UHPC-NC bonding tests conducted by Muñoz et al. [12], Zhao et al. [47], Jafarinejad et al. [48], and Zhang et al. [49] are also simulated using the FE models. Figure 13b depicts the comparative analysis between the experimental and numerical results of the shear strength of the UHPC-NC bond interface, indicating that the use of the CZM exhibits high accuracy in the simulation of the UHPC-NC bond interface.

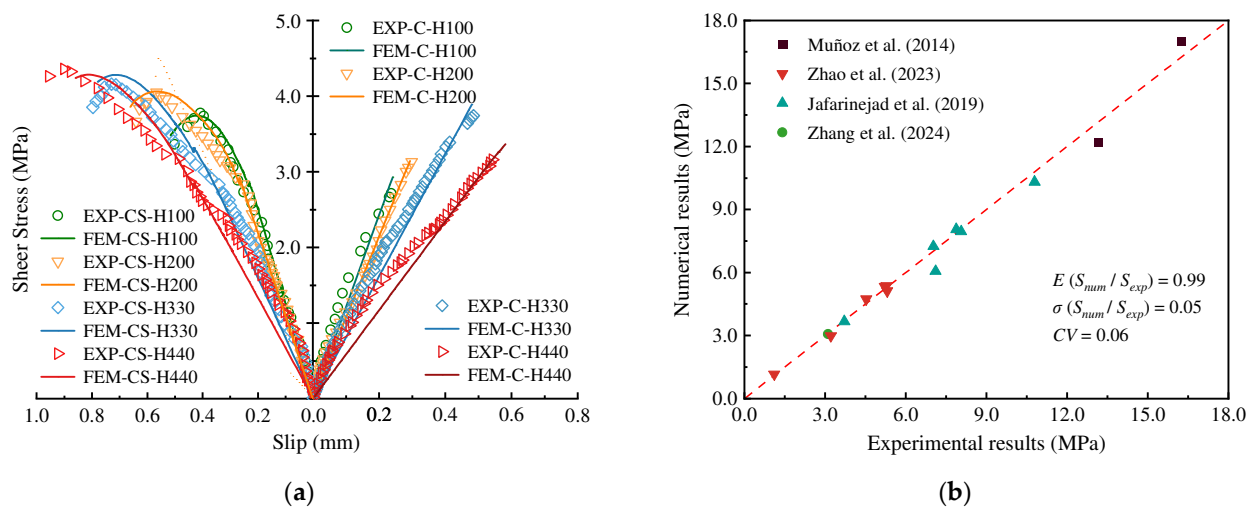


Figure 13. Comparison of experimental and numerical results: (a) the C and CS specimens and (b) external data validation [12,47–49].

5.2. Stress Field on the UHPC-NC Interface with Varying Heights

5.2.1. Stress Distribution Along the Interface

The shear stress field at the interface was obtained from FE models to study the size effects in the UHPC-NC interface. Figure 14 illustrates the shear stress distribution along the interface height at a shear stress level of 1.0 MPa and 2.0 MPa. The shear stress distribution along the interface is non-uniform, with higher values at the ends and lower values at the center. The discrepancy between the maximum and minimum shear stress becomes more pronounced as the interface size increases. A non-uniformity coefficient (φ) is introduced to quantify unevenness, defined as the ratio of the difference between the maximum and minimum shear stress to the average shear stress. Upon achieving the average shear stress of 1.0 MPa, the calculations indicate that the φ values for the chiseled

interface with bonding heights of 100 mm, 200 mm, 330 mm, and 440 mm are 1.7%, 7.6%, 16.3%, and 18.0%, respectively. Furthermore, the ϕ values for the chiseled interface with additional steel rebars are 1.2%, 4.8%, 12.0%, and 17.4%, in that order. In the 2.0 MPa scenario, the ϕ values retain similarity to the previous values, while indicating that an increased bonding height significantly exacerbates stress non-uniformity, which persists throughout the loading process. However, incorporating interfacial shear rebars has been observed to homogenize the shear stress distribution at the interface. In addition, the numerical results similarly report the presence of a small amount of normal stress at the interface under shear, which suggests that although the bond interface of the direct shear specimens is primarily subject to shear forces, it is also subjected to a complex stress state involving both shear compression and tensile forces. As a result, it is advisable to subject the bond surface to roughening treatment before the implantation of shear steel rebars, which is in line with recommended engineering procedures.

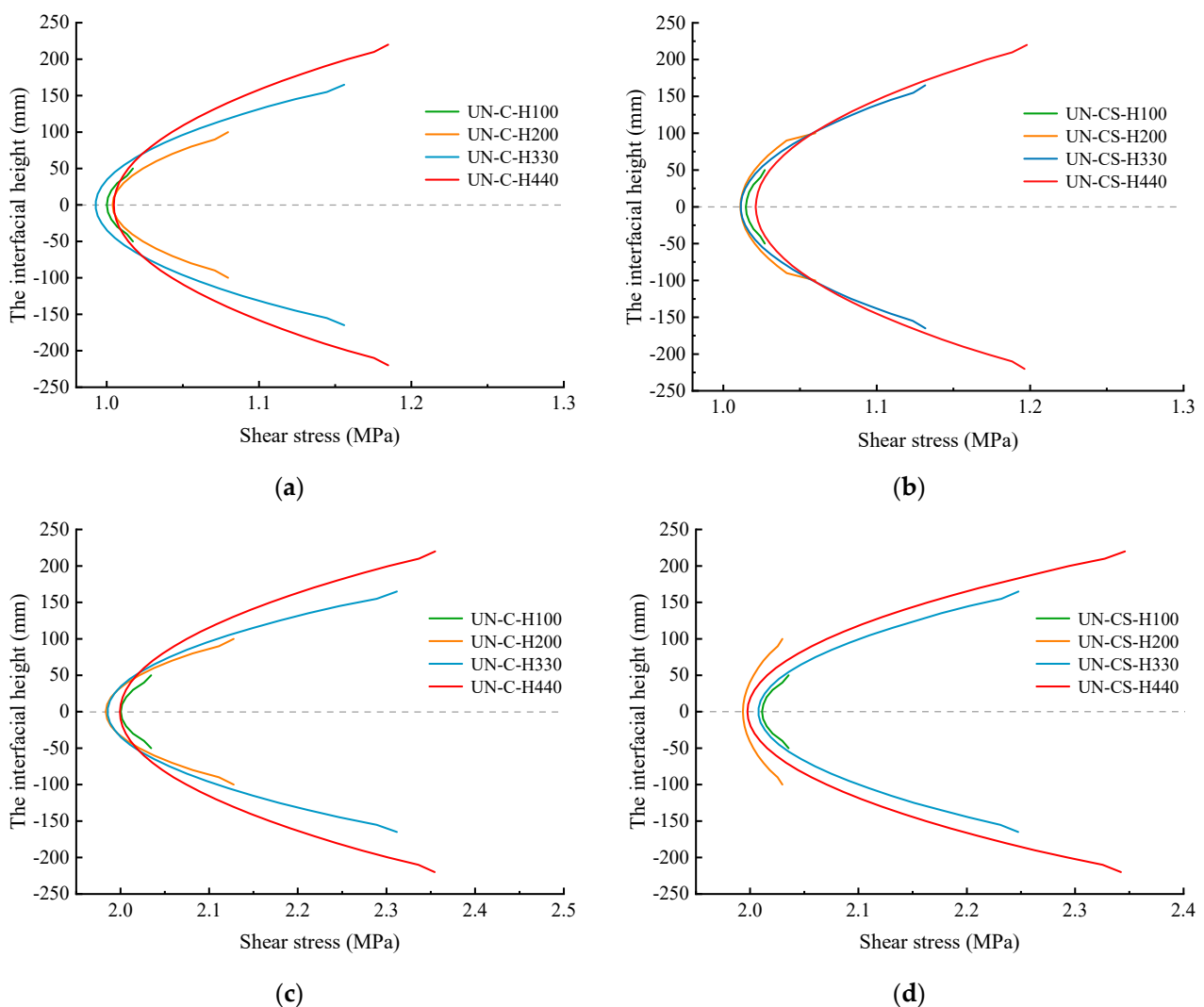


Figure 14. Shear stresses distribution along the interface height: (a) 1.0 MPa (Series C); (b) 1.0 MPa (Series CS); (c) 2.0 MPa (Series C); (d) 2.0 MPa (Series CS).

Figure 15 illustrates the principal tensile stress in the concrete at the shear transition zone between the UHPC and NC. The CS specimens demonstrate a more pronounced concentration of principal stresses than the C specimens, especially in the concrete surrounding the steel rebars. This effectively restrains transverse separation during loading, corresponding to the slower cracking process observed in the CS specimens. The presence

of rebars facilitates stress redistribution during cracking, particularly in larger specimens where the size effect is more significant. Larger specimens tend to exhibit higher stress concentrations near the rebars, leading to earlier cracking. This reveals the relatively lower cracking strength of the CS specimens. As the interface height increases, stress concentration around the rebars intensifies, rendering larger specimens more susceptible to early cracking despite the overall improvement in shear capacity. Therefore, while the rebars enhance bond interface performance, their effectiveness is influenced by specimen size, which is an important consideration in design applications.

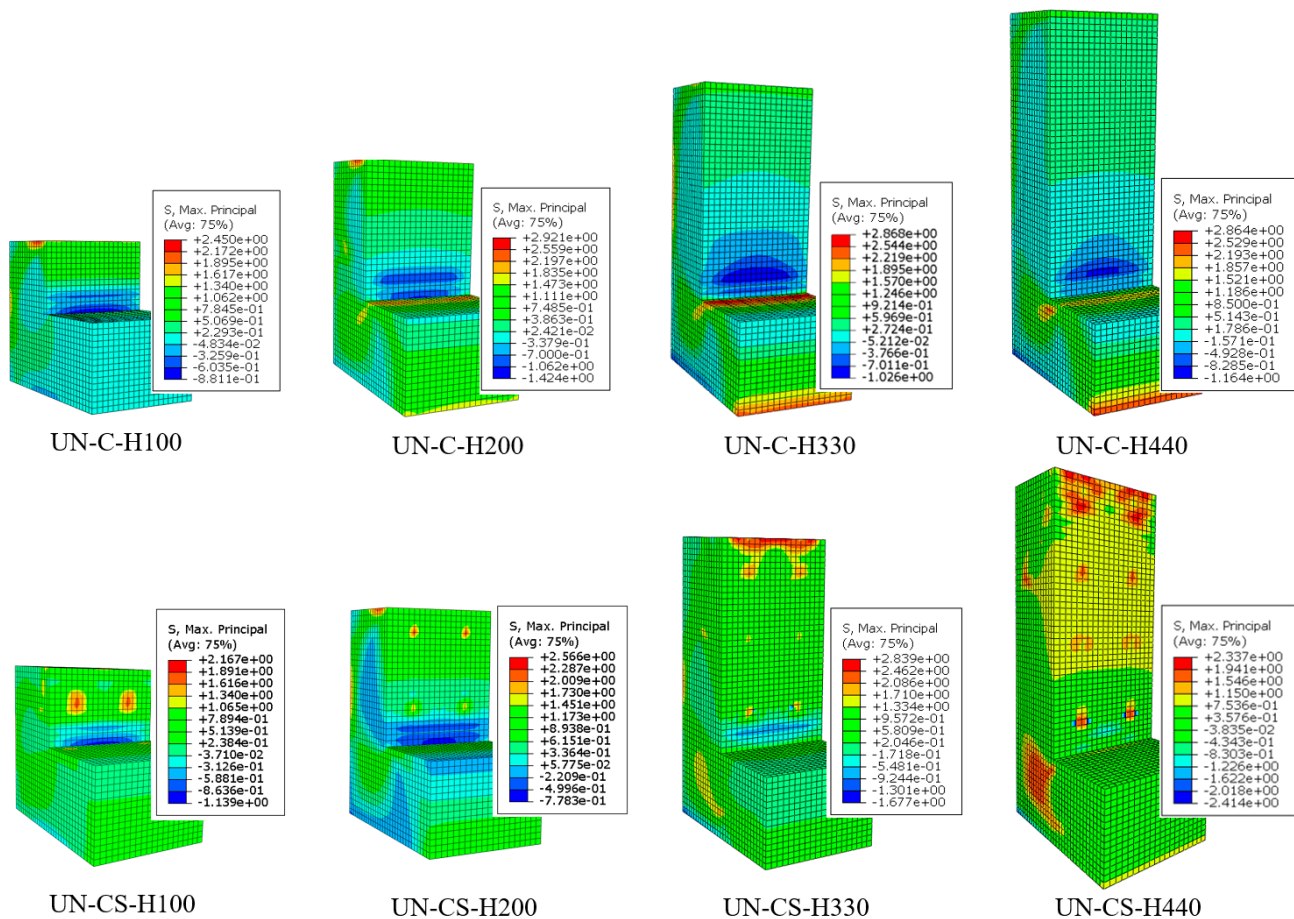


Figure 15. Max principal stress of the direct shear specimens.

5.2.2. Shear Bond Evolution in the UHPC-NC Interface with Varying Heights

Figure 16 presents the distribution of interfacial shear stress between UHPC and NC under varying interface heights. As interface height increases, shear stress across the bonding interface becomes progressively uneven, especially in shorter specimens ($H = 100$ mm and 200 mm), where stress concentrations shift toward the lower interface edge with rising load. In taller specimens ($H = 330$ mm and 440 mm), stress consistently decreases toward the central region while increasing toward the extremities. This pattern indicates a pronounced size effect, with smaller interfaces more susceptible to stress concentration and non-uniform distribution. In CS specimens, shear rebars significantly alter the stress distribution, shifting the peak stress region toward the specimen's midpoint. Moreover, rebars positioned nearer the loaded end exhibit a heightened capacity to resist higher shear stresses. Shear rebars thus mitigate specimen size effects, enhancing stress redistribution and load transfer efficiency, particularly in smaller specimens. Across various interface heights, the introduction of shear rebars shifts high-stress regions toward the upper and middle portions of the interface. In larger specimens ($H = 330$ mm and 440 mm), the initial stress distribution is more uniform, and the inclusion of rebars further transforms the shear

stress pattern, optimizing load transfer and reducing size-induced stress concentration. In both C and CS specimens, variations in UHPC-NC bond interface height under external load result in a non-uniform distribution and the transfer of shear stresses. These findings suggest a potential correlation between specimen size and shear mechanical response, highlighting the role of shear rebars in controlling stress distribution and performance across interfaces.

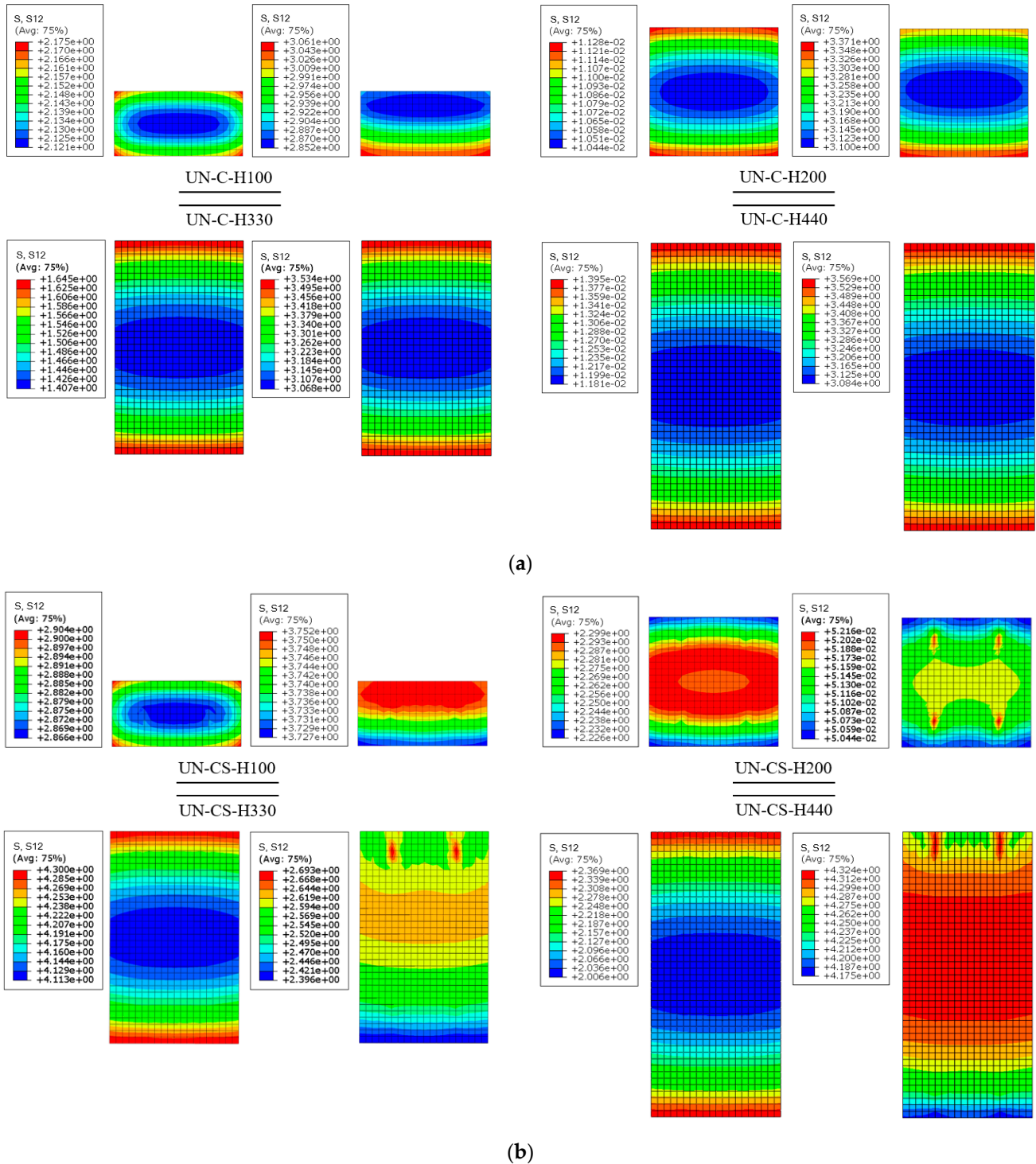


Figure 16. Shear stress distribution of the cohesive element: (a) Series C and (b) Series CS.

To investigate the degradation mechanism at the bond interface between UHPC and NC, cohesive elements in the CZM were extracted for damage analysis. The focus was on the quadratic nominal stress criterion. The QUADSCRT variable indicates cohesive failure when it reaches 1, while the Scalar Stiffness Degradation (SDEG) parameter in ABAQUS shows stiffness reduction, with 0 indicating no damage and 1 indicating complete damage [50,51].

Figure 17 illustrates the evolution of damage along the UHPC-NC bond interface at various heights under loading. Figure 17a,b provide a three-dimensional representation, clarifying how damage evolves along the interface height as shear stress changes. As shear stress increases, the interfacial damage contour curves, reflecting the stress distribution along the interface height. Damage levels are directly proportional to interface stress, with shear stress introducing inhomogeneity in the interfacial damage. This inhomogeneity progressively intensifies with increased loading. Throughout the loading process, the maximum difference between peak and minimum values of the QUADSCRT in C-series specimens with interface heights of 100 mm, 200 mm, 330 mm, and 440 mm is 0.03, 0.12, 0.26, and 0.28, respectively, while for CS-series specimens, the values are 0.02, 0.08, 0.18, and 0.25, respectively. These results indicate that larger interface sizes result in more significant inhomogeneity of interfacial damage. While increasing the interface size may enhance shear strength, this increased inhomogeneity could inhibit further mechanical property improvement by decelerating the growth in strength. Figure 17c shows the dynamic evolution of interfacial damage in both C and CS series specimens, using a specimen with a 200 mm interface height as a case study to illustrate damage evolution at a consistent stress level. Observations indicate that damage initiates at the interface ends and propagates toward the center. In C-series specimens, damage evolution is more pronounced compared to CS-series specimens under equivalent stress conditions. In the CS specimens, damage development in the highlighted region shows significant improvement over the C specimens. This finding suggests that, while the initial damage onset is similar for both series, the incorporation of steel rebars in CS specimens exerts a delaying effect on damage progression. This reinforcement enhances the mechanical performance of the interface by mitigating the size effect and delaying crack propagation. Consequently, CS specimens exhibit a more sustained response and delayed crack progression under external loading.

The degradation and damage of the UHPC-NC bond interface generally unfold in three sequential stages. In the initiation stage, damage and stiffness degradation begin at the interface's upper and lower ends. This is followed by the propagation stage, where the damage spreads toward the center of the interface. Finally, in the failure stage, the behavior diverges based on the specimen type; C specimens experience rapid failure following propagation, whereas CS specimens exhibit a slower degradation process. In CS specimens, a degradation zone gradually forms around the rebars after the initial failure at the ends, eventually leading to a total loss of stiffness.

The degradation of interface stiffness progresses alongside damage generation, as shown in Figure 18, which presents the evolution of interface stiffness under loading for a series of specimens subjected to a uniform analysis step. In these figures, specimens of varying interface heights are ordered hierarchically within each analysis step. The onset of stiffness degradation occurs later in specimens with larger interface sizes, highlighting the size effect. For the C-series specimens, stiffness degradation initially proceeds in a nearly linear manner, with rapid early-stage growth. The SDEG values of the interfaces for the 100 mm, 200 mm, 330 mm, and 440 mm specimens are 0.697, 0.613, 0.496, and 0.458, respectively, showing a consistent downward trend. In contrast, for the CS-series specimens, the trend in stiffness degradation for smaller interfaces resembles that of the C-series, while larger interface specimens show a more gradual progression, marked by an increase in the fold line height. This gradual increase may be due to the longer path required for transmitting internal forces in taller specimens, allowing for greater utilization of shear reinforcement properties, which improves the initial phase of stiffness degradation. These observations suggest that incorporating reinforcement bars within larger UHPC-NC

bond interfaces can effectively delay damage and mitigate stiffness degradation, enhancing the overall durability of the interface.

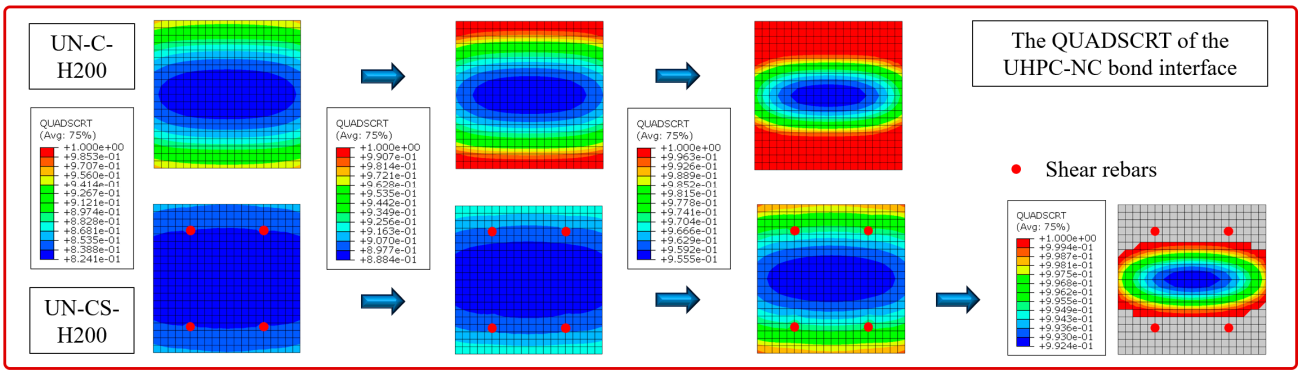
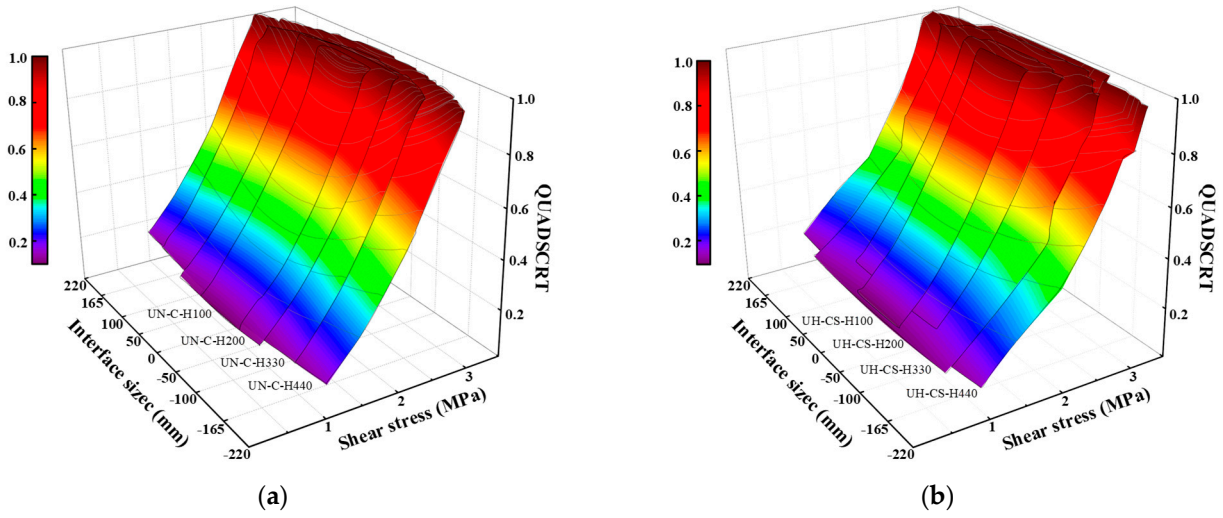


Figure 17. Damage evolution of the UHPC-NC bond interface: (a) Series C; (b) Series CS; (c) damage process of UN-C-H200 and UN-CS-H200.

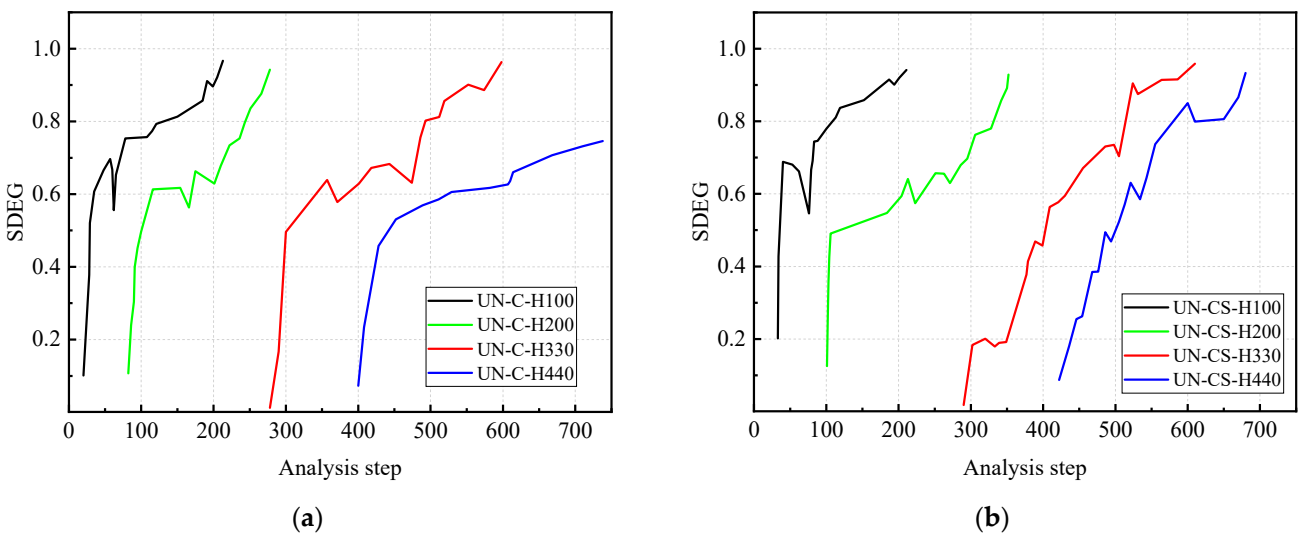


Figure 18. SDEG of the UHPC-NC bond interface: (a) Series C and (b) Series CS.

6. Conclusions

This paper presents a comprehensive study of the size effect and shear properties of UHPC-NC bond interfaces, employing both experimental and FE methods. The mechanical behaviors and responses, including failure modes, load–displacement relationships, and strain histories, were discussed in detail based on the test results. Furthermore, FE models of the direct shear specimens were constructed and calibrated using CZM, and a comprehensive analysis was conducted to investigate the stress field distribution and damage degradation at the bond interface. The main conclusions are as follows:

(1) The bond interface with roughening treatment showed brittle damage. Smaller interface heights mostly failed in mode (P), while larger heights failed in mode (F). Adding rebars improved performance, resulting in more ductile damage and predominantly mode (P) failures. The rebars redistributed stresses, boosting mechanical interlock and friction on the rough surface, and lessening the shear stress impact on the NC substrate. This effect was more pronounced in specimens with smaller interfaces, highlighting a size effect in the stress distribution and failure mode.

(2) Shear strength, slip, and stiffness showed size effects as the bond interface height changed. Shear strength and slip increased with greater interface height, while shear stiffness exhibited a decreasing trend. The incorporation of steel rebars at the interface mitigates the size effect and facilitates effective shear load transfer. This enhances the distribution of shear stresses between the concrete blocks and extends the interfacial fracture process.

(3) The cohesive elements' stress field and damage progression were analyzed. The shear stress distribution along the interface exhibited a size-dependent gradient, with larger interface heights showing more pronounced stress concentration at the ends compared to smaller interfaces. Implanting rebars mitigated this uneven distribution, particularly in specimens with smaller interface heights. The region encircled by the rebars in the CS specimens exhibited a more gradual damage progression, enhancing interfacial stiffness and reducing the susceptibility to damage, especially in specimens with shorter interfaces.

Author Contributions: Conceptualization, S.H.; data curation, S.H., X.H., J.H., Z.W. and Z.Y.; formal analysis, X.H. and J.H.; funding acquisition, S.H. and Y.Z.; investigation, X.H., J.H. and Z.W.; methodology, S.H. and X.H.; project administration, Z.Y.; resources, S.H.; software, X.H. and J.H.; supervision, Y.Z., Z.W. and Z.Y.; validation, S.H., X.H., J.H., Y.Z. and Z.Y.; visualization, Z.W.; writing—original draft, X.H.; writing—review and editing, S.H. and Y.Z. All authors have read and agreed to the published version of the manuscript.

Funding: This research was funded by the National Natural Science Foundation of China (Grant # 52278161, and Grant # 52108174), the Guangdong Basic and Applied Basic Research Foundation (Grant # 2023A1515010535), and the Science and Technology Project of Guangzhou (Grant # 2024A04J9888).

Data Availability Statement: The original contributions presented in the study are included in the article, further inquiries can be directed to the corresponding author.

Acknowledgments: The authors would like to thank all the anonymous referees for their constructive comments and suggestions.

Conflicts of Interest: Author Zhiyong Wan was employed by the company Guangdong Communication Planning & Design Institute Group Co., Ltd. The remaining authors declare that the research was conducted in the absence of any commercial or financial relationships that could be construed as a potential conflict of interest.

References

1. Zaki, Y.A.; Abouhussien, A.A.; Hassan, A.A.A.; Ismail, M.K.; AbdelAleem, B.H. Crack detection and classification of repaired concrete beams by acoustic emission monitoring. *Ultrasonics* **2023**, *134*, 107068. [[CrossRef](#)] [[PubMed](#)]
2. Ismail, M.K.; Hassan, A.A. Structural performance of large-scale concrete beams reinforced with cementitious composite containing different fibers. *Structures* **2021**, *31*, 1207–1215. [[CrossRef](#)]

3. Hu, J.; Zou, C.; Liu, Q.; Li, X.; Tao, Z. Floor vibration predictions based on train-track-building coupling model. *J. Build. Eng.* **2024**, *89*, 109340. [[CrossRef](#)]
4. Hanif, M.U.; Ibrahim, Z.; Ghaedi, K.; Hashim, H.; Javanmardi, A. Damage assessment of reinforced concrete structures using a model-based nonlinear approach—A comprehensive review. *Constr. Build. Mater.* **2018**, *192*, 846–865. [[CrossRef](#)]
5. Abellán-García, J.; Carvajal-Muñoz, J.S.; Ramírez-Munévar, C. Application of ultra-high-performance concrete as bridge pavement overlays: Literature review and case studies. *Constr. Build. Mater.* **2024**, *410*, 134221. [[CrossRef](#)]
6. Graybeal, B.; Brühwiler, E.; Kim, B.-S.; Toutlemonde, F.; Voo, Y.L.; Zaghi, A. International perspective on UHPC in bridge engineering. *J. Bridge Eng.* **2020**, *25*, 04020094. [[CrossRef](#)]
7. Fathy, A.; Zhu, H.; Kohail, M. Factors affecting the fresh-to-hardened concrete repair system. *Constr. Build. Mater.* **2022**, *320*, 126279. [[CrossRef](#)]
8. Haber, Z.B.; Foden, A.; McDonagh, M.; Ocel, J.; Zmetra, K.; Graybeal, B. *Design and Construction of UHPC-Based Bridge Preservation and Repair Solutions (No. FHWA-HRT-22-065)*; Federal Highway Administration, Office of Infrastructure Research and Development: Washington, DC, USA, 2022. [[CrossRef](#)]
9. Kennedy, D.; Habel, K.; Fraser, G. Ultra high-performance concrete column jacket retrofit for the mission bridge. In Proceedings of the 11th Canadian Conference on Earthquake Engineering, Victoria, BC, Canada, 21–24 July 2015.
10. Song, X.; Song, X.; Liu, H.; Huang, H.; Anvarovna, K.G.; Ugli, N.A.D.; Huang, Y.; Hu, J.; Wei, J.; Yu, Q. Cement-based repair materials and the interface with concrete substrates: Characterization, evaluation and improvement. *Polymers* **2022**, *14*, 1485. [[CrossRef](#)]
11. Garbacz, A.; Piotrowski, T.; Courard, L.; Kwaśniewski, L. On the evaluation of interface quality in concrete repair system by means of impact-echo signal analysis. *Constr. Build. Mater.* **2017**, *134*, 311–323. [[CrossRef](#)]
12. Muñoz, M.A.C.; Harris, D.K.; Ahlborn, T.M.; Froster, D.C. Bond performance between ultrahigh-performance concrete and normal-strength concrete. *J. Mater. Civ. Eng.* **2014**, *26*, 04014031. [[CrossRef](#)]
13. ACI Committee 546. *Guide for the Selection of Materials for the Repair of Concrete*; American Concrete Institute: Indianapolis, IN, USA, 2006.
14. Yu, J.; Zhang, B.; Chen, W.; Liu, H.; Li, H. Multi-scale study on interfacial bond failure between normal concrete (NC) and ultra-high performance concrete (UHPC). *J. Build. Eng.* **2022**, *57*, 104808. [[CrossRef](#)]
15. Apostolinas, V.G.; Galopoulou, K.S.; Kouris, L.A.S.; Anastasiou, E.K.; Konstantinidis, A.A. Experimental investigation and analytical modelling of the roughness and bonding agent influence on the old-to-repair concrete interfacial bonding strength. *Mater. Struct.* **2022**, *55*, 148. [[CrossRef](#)]
16. Zhang, Y.; Zhu, P.; Liao, Z.; Wang, L. Interfacial bond properties between normal strength concrete substrate and ultra-high performance concrete as a repair material. *Constr. Build. Mater.* **2020**, *235*, 117431. [[CrossRef](#)]
17. Farzad, M.; Shafieifar, M.; Azizinamini, A. Experimental and numerical study on bond strength between conventional concrete and Ultra High-Performance Concrete (UHPC). *Eng. Struct.* **2019**, *186*, 297–305. [[CrossRef](#)]
18. Bažant, Z.P.; Planas, J. *Fracture and Size Effect in Concrete and Other Quasibrittle Materials*; Routledge: London, UK, 2019. [[CrossRef](#)]
19. Su, J. The Research on the Size Effect of Concrete Behavior in Compression and Tension. Ph.D. Thesis, Hunan University, Changsha, China, 2012. (In Chinese).
20. Bažant, Z.P. Size effect on structural strength: A review. *Arch. Appl. Mech.* **1999**, *69*, 703–725. [[CrossRef](#)]
21. Jaber, H.T.; Sarsam, K.F.; Muhammad, B.R. Literature review on size effect of shear reinforced concrete beams. *AIP Conf. Proc.* **2023**, *2651*, 020006. [[CrossRef](#)]
22. Rios, R.D.; Riera, J.D. Size effects in the analysis of reinforced concrete structures. *Eng. Struct.* **2004**, *26*, 1115–1125. [[CrossRef](#)]
23. Fang, Z.; Wu, R.J.; Pei, B.Z.; Jiang, Z.-W. Size effect of the shear performance on the bonding interface between new and old concrete. *China J. Highw. Transp.* **2021**, *34*, 92–103. (In Chinese) [[CrossRef](#)]
24. He, S.; Huang, X.; Zhong, H.; Wan, Z.; Liu, G.; Xin, H.; Zhang, Y. Experimental study on bond performance of UHPC-to-NC interfaces: Constitutive model and size effect. *Eng. Struct.* **2024**, *317*, 118681. [[CrossRef](#)]
25. *GB/T 31387-2015*; Reactive Powder Concrete. AQSIQ & SAC (General Administration of Quality Supervision, Inspection and Quarantine of the People's Republic of China & Standardization Administration of the People's Republic of China); Standards Press of China: Beijing, China, 2015.
26. *GB/T 50081-2019*; Concrete Physical and Mechanical Properties Test Methods Standard. MOHURD & AQSIQ (Ministry of Housing and Urban-Rural Development of the People's Republic of China & General Administration of Quality Supervision, Inspection and Quarantine of the People's Republic of China); China Architecture & Building Press: Beijing, China, 2019.
27. *GB/T 14902-2012*; Ready-Mixed Concrete. AQSIQ & SAC (General Administration of Quality Supervision, Inspection and Quarantine of the People's Republic of China & Standardization Administration of the People's Republic of China); Standards Press of China: Beijing, China, 2012.
28. *GB/T 228.1-2010*; Metallic Materials-Tensile Testing-Part 1: Method of Test at Room Temperature. AQSIQ & SAC (General Administration of Quality Supervision, Inspection and Quarantine of the People's Republic of China & Standardization Administration of the People's Republic of China); Standards Press of China: Beijing, China, 2010.
29. Shah, S.G.; Kishen, J.C. Nonlinear fracture properties of concrete–concrete interfaces. *Mech. Mater.* **2010**, *42*, 916–931. [[CrossRef](#)]
30. Zhang, B.S.; Yu, J.J.; Chen, W.Z.; Chen, J.; Li, H.; Niu, J. Interface shear failure behavior between normal concrete (NC) and ultra-high performance concrete (UHPC). *Int. J. Concr. Struct. Mater.* **2024**, *18*, 18. [[CrossRef](#)]

31. Al-Fasih, M.Y.; Mohamad, M.E.; Ibrahim, I.S.; Ahmad, Y.; Ariffin, M.A.M.; Sarbini, N.N.; Mohamed, R.N.; Kueh, A.B.H. Experimental and numerical evaluations of composite concrete-to-concrete interfacial shear strength under horizontal and normal stresses. *PLoS ONE* **2021**, *16*, e0252050. [[CrossRef](#)] [[PubMed](#)]
32. Xia, J.; Shan, K.-Y.; Wu, X.-H.; Gan, R.-L.; Jin, W.-L. Shear-friction behavior of concrete-to-concrete interface under direct shear load. *Eng. Struct.* **2021**, *238*, 112211. [[CrossRef](#)]
33. Zhang, Y.; Zhu, P.; Wang, X.; Wu, J. Shear properties of the interface between ultra-high performance concrete and normal strength concrete. *Constr. Build. Mater.* **2020**, *248*, 118455. [[CrossRef](#)]
34. Zhang, W.; Yan, B.; Ye, Y.; Yi, W. Direct shear test study on old and new concrete. *J. Build. Eng.* **2024**, *82*, 108391. [[CrossRef](#)]
35. Daneshvar, D.; Behnood, A.; Robisson, A. Interfacial bond in concrete-to-concrete composites: A review. *Constr. Build. Mater.* **2022**, *359*, 129195. [[CrossRef](#)]
36. Khoramishad, H.; Crocombe, A.; Katnam, K.; Ashcroft, I. Fatigue damage modelling of adhesively bonded joints under variable amplitude loading using a cohesive zone model. *Eng. Fract. Mech.* **2011**, *78*, 3212–3225. [[CrossRef](#)]
37. Xu, Z.M.; Huang, Y. Finite element analysis of progressive collapse resistance of precast concrete frame beam-column substructures with UHPC connections. *J. Build. Eng.* **2024**, *82*, 108338. [[CrossRef](#)]
38. Wang, X.; Liu, Z.; Tong, T.; Wu, D. Bond-slip behavior of deformed rebar in grouted duct connection: Experiment, theoretical analysis and cohesive-zone element model. *Constr. Build. Mater.* **2024**, *421*, 135694. [[CrossRef](#)]
39. Zhang, Z.; Shao, X.D.; Li, W.G.; Ping, Z.; Hong, C. Axial tensile behavior test of ultra high performance concrete. *China J. Highw. Transp.* **2015**, *28*, 50–58. (In Chinese) [[CrossRef](#)]
40. AFGC (Association Française de Génie Civil). *Ultra High Performance Fiber Reinforced*; AFGC (Association Française de Génie Civil): Paris, France, 2013.
41. Ding, F.X.; Yu, Z.W. Unified calculation method of mechanical properties of concrete in tension. *J. Civ. Eng. Manag.* **2004**, *21*, 29–34. (In Chinese) [[CrossRef](#)]
42. Yu, Z.W.; Ding, F.X. Unified calculation method of compressive mechanical properties of concrete. *J. Build. Struct.* **2003**, *24*, 41–46. (In Chinese) [[CrossRef](#)]
43. He, S.; Yang, G.; Zhou, W.; Li, Q.; Dong, Y. Evaluation of shear lag effect in HSS-UHPC composite beams with perfobond strip connectors: Experimental and numerical studies. *J. Constr. Steel Res.* **2022**, *194*, 107312. [[CrossRef](#)]
44. Li, S.; Liu, W.; Sun, W.; Hou, S. Effects of adherend notching on the bonding performance of composite single-lap joints. *Eng. Fract. Mech.* **2023**, *81*, 109141. [[CrossRef](#)]
45. Mi, Y.; Crisfield, M.A.; Davies, G.A.O.; Hellweg, H.B. Progressive delamination using interface elements. *J. Compos. Mater.* **1998**, *32*, 1246–1272. [[CrossRef](#)]
46. Han, X.; Hu, M.; Wang, Y.; Liu, B.; da Silva, L.F.; Guo, X. Experiments and modelling of competitive failure behaviour of CFRP stepped-lap repairs with different design parameters. *Thin-Walled Struct.* **2024**, *199*, 111836. [[CrossRef](#)]
47. Zhao, Y.-C.; Lei, H.-G.; Guo, L.-K.; Lu, G.-Y. Experimental investigation on interface performance of uhpc-strengthened nc structure through push-out tests. *Materials* **2023**, *16*, 1766. [[CrossRef](#)]
48. Jafarinejad, S.; Rabiee, A.; Shekarchi, M. Experimental investigation on the bond strength between ultra high strength fiber reinforced cementitious mortar & conventional concrete. *Constr. Build. Mater.* **2019**, *229*, 116814. [[CrossRef](#)]
49. Zhang, Y.; Wu, Y.; Qin, Y.; Zhu, Y.; Qiu, J.; Wang, W. Experimental and analytical study on interfacial shear resistance of prefabricated ultra-high performance concrete-post-cast normal concrete interface. *Adv. Struct. Eng.* **2024**, *27*, 1622–1634. [[CrossRef](#)]
50. Wang, Y.; Feng, Y.; Deng, J.; Cai, W.; Wang, K.; Ma, C.; Wanyan, Q.; Li, K.; Bai, S.; Li, H. Integrated experimental and numerical study on debonding of cement-casing interface. In Proceedings of the ARMA US Rock Mechanics/Geomechanics Symposium, Santa Fe, NM, USA, 26–29 June 2022.
51. Zhang, Y.; Cheng, Z.Y.; Jia, Z.K. Failure loads analysis of corroded pipe repaired by composite material under tension and internal pressure. *J. Mar. Eng. Technol.* **2022**, *21*, 178–188. [[CrossRef](#)]

Disclaimer/Publisher’s Note: The statements, opinions and data contained in all publications are solely those of the individual author(s) and contributor(s) and not of MDPI and/or the editor(s). MDPI and/or the editor(s) disclaim responsibility for any injury to people or property resulting from any ideas, methods, instructions or products referred to in the content.